International Journal of Innovative Information Systems & Technology Research 14(3):105-125, July-Sept, 2026

© SEAHI PUBLICATIONS, 2026 www.seahipublications.org ISSN: 2467-8562

DOI:10.5281/zenodo.21380995

Development of Computer-Based Analytical Techniques for the Characterization and Modelling of Locally Synthesized Nanomaterials for Energy and Electronic Applications

Musa Aliyu[1]; Muftahu Sulaiman[2]; Jamilu Yusuf K/Sauri[3]; Abubakar Sadiq Usman[4] & Abubakar Ibn Abubakar[5]

[1&5]Department of Computer Hardware Engineering Technology
School of Technology
Katsina State Institute of Technology and Management, Katsina, Nigeria

[2&3]Department of Electrical and Electronic Engineering
School of Technology
Katsina State Institute of Technology and Management, Katsina, Nigeria

[4]Department of Multi media Technology
School of Technology
Katsina State Institute of Technology and Management, Katsina, Nigeria

Corresponding author e-mails: musa.aliyu@ksitm.edu.ng , aliyumusa07@gmail.com

ABSTRACT

The rapid advancement of nanomaterials has significantly transformed energy and electronic technologies by enabling enhanced efficiency, miniaturization, and multifunctionality of devices. Despite these advances, a major challenge remains in the accurate characterization and predictive modelling of nanomaterials, particularly those synthesized locally in developing research environments. Conventional experimental techniques often generate complex datasets whose full potential is underutilized due to limited computational analysis and integration. This study therefore focuses on the Development of computer-based analytical techniques for the characterization and modelling of locally synthesized nanomaterials for energy and electronic applications. The proposed research aims to design and implement robust computational frameworks that integrate experimental characterization data with advanced numerical analysis, simulation tools, and data-driven modelling approaches. Experimental data obtained from techniques such as X-ray diffraction (XRD), Fourier transform infrared spectroscopy (FTIR), Raman spectroscopy, scanning and transmission electron microscopy (SEM/TEM), and electrical measurements will be systematically analyzed using customized algorithms and modelling software. These tools will enable the extraction of key material parameters, including crystallite size, phase composition, defect density, band structure, charge transport characteristics, and thermal stability, with improved accuracy and reproducibility. Furthermore, the study will develop predictive models that establish quantitative relationships between synthesis conditions, microstructural features, and functional

performance of nanomaterials in energy and electronic devices such as photovoltaic cells, energy storage systems, and nanoscale sensors. By combining physics-based simulations with statistical and machine learning techniques, the research will provide a reliable platform for performance prediction and optimization without excessive experimental trial-and-error. The expected outcomes of this work include automated and standardized computer-based analytical pipelines, validated modelling tools for nanomaterial performance prediction, and optimized material design strategies suitable for local production. Scientifically, the study will contribute to improved understanding of structure–property–performance relationships in nanomaterials, while technologically it will enhance local research capacity and promote cost-effective innovation in energy and electronic applications. Overall, the project is expected to accelerate nanomaterials research and device development through the effective integration of computational analytics with experimental characterization, making it suitable for dissemination in peer-reviewed scientific journals.

Keywords: nanomaterials, nanoscale sensors, electronic technologies

INTRODUCTION

Nanomaterials exhibit unique size-dependent properties, including enhanced surface area, quantum confinement, and tunable electrical and optical behavior, making them ideal candidates for applications in solar cells, batteries, supercapacitors, sensors, and nanoelectronics (Cao, 2020). Despite their potential, the adoption and optimization of nanomaterials in Nigeria are hindered by challenges in experimental characterization and predictive modelling.

Recent advances in computational methods, including Density Functional Theory (DFT), Molecular Dynamics (MD), and Finite Element Analysis (FEA), enable accurate prediction of nanomaterials' properties and behavior under varying conditions. Integrating computer-based analytical techniques with laboratory synthesis can accelerate the design of functional nanomaterials, optimize their properties, and support energy and electronics applications without extensive experimental trials (Gupta & Singh, 2021).

Nanomaterials possess unique size-dependent properties, such as enhanced surface area, quantum confinement effects, and tunable electronic and optical behavior, which make them highly suitable for energy and electronic applications. Despite their potential, the practical utilization of locally synthesized nanomaterials in Nigeria remains limited. This limitation is largely due to insufficient computational and analytical tools capable of accurately characterizing and predicting their physicochemical properties. Most Nigerian laboratories rely on conventional experimental techniques, which are often costly, time-consuming, and unable to fully capture nanoscale phenomena.

Furthermore, the lack of integrated computational workflows prevents researchers from effectively correlating experimental observations with theoretical models, hindering the optimization of nanomaterials for specific applications such as solar energy conversion, battery development, and electronic devices. Additionally, the reliance on imported commercial software for nanomaterial modeling increases research costs and limits accessibility for local institutions. Consequently, there is a pressing need to develop **locally adaptable, computer-based analytical techniques** that can reliably characterize and model nanomaterials, thereby bridging the gap between synthesis and practical application and enhancing Nigeria's capacity in energy and electronic nanotechnology research.

The main aim of this research work is to develop computer-based analytical techniques for the characterization and modeling of locally synthesized nanomaterials, enhancing their application in energy and electronic device with the following specific objectives:

1. To synthesize selected nanomaterials locally using eco-friendly and cost-effective methods
2. To develop computer-based workflows for structural, optical, and electronic characterization
3. To simulate and model nanomaterial properties using computational tools such as DFT and MD
4. To validate computational models with experimental data
5. To create a database of locally synthesized nanomaterials and their predicted properties

Nanomaterials have emerged as key components in energy storage, photovoltaics, and electronic devices due to their high surface-to-volume ratio and quantum confinement effects (Cao, 2020). Traditional

characterization techniques—X-ray diffraction (XRD), Fourier-transform infrared spectroscopy (FTIR), scanning electron microscopy (SEM), and UV-Vis spectroscopy—provide essential insights into structural, optical, and morphological properties. However, interpreting these results and predicting device performance often require computational approaches (Gupta & Singh, 2021).

Computational modelling techniques such as Density Functional Theory (DFT), Molecular Dynamics (MD), and Finite Element Analysis (FEA) allow prediction of electronic band structure, optical properties, and mechanical stability of nanomaterials. For example, DFT simulations have been widely used to predict electronic energy levels in metal oxide and perovskite nanostructures, enabling design optimization before experimental fabrication (Kumar et al., 2019). MD simulations complement this by evaluating temperature-dependent stability, ion migration, and nanoscale interactions in energy storage materials (Zhang et al., 2021).

Hybrid approaches combining experimental synthesis with computational modeling improve efficiency in material optimization and reduce time-to-deployment in electronic and energy devices. Yet, in Nigeria, there is limited adoption of integrated computational-experimental workflows. Most studies are either purely experimental or rely on imported commercial software, creating barriers to cost-effective local research. This highlights the need for locally developed computer-based analytical techniques that can simulate, model, and predict the behavior of nanomaterials synthesized in Nigerian laboratories.

Research Gap: While global studies demonstrate the effectiveness of computational modelling in nanomaterials research, Nigeria currently lacks integrated computational-experimental workflows for locally synthesized nanomaterials. There is a need for low-cost, adaptable, and validated computer-based techniques that can predict and correlate nanomaterial properties for energy and electronics applications.

MATERIALS AND METHODS

Research Design

This study adopted a quantitative experimental–computational research design to develop an integrated computer-based analytical framework for the characterization and modelling of locally synthesized nanomaterials intended for energy and electronic applications. The research combined laboratory synthesis, advanced materials characterization, computational signal processing, digital image analysis, machine learning, and statistical modelling into a unified workflow. The overall methodology comprised six sequential stages: (i) synthesis of semiconductor nanomaterials using locally available precursor materials; (ii) structural, morphological, optical, and electrical characterization; (iii) acquisition and preprocessing of characterization datasets; (iv) development of computer-based analytical algorithms for automated feature extraction. This integrated approach was designed to reduce human intervention in data interpretation while improving analytical accuracy, repeatability, and computational efficiency.

Materials

Analytical-grade chemicals were used throughout this investigation to ensure high reproducibility and minimize contamination during synthesis. Zinc nitrate hexahydrate ($Zn(NO_3)_2 \cdot 6H_2O$, 99.9%) was employed as the zinc precursor, while sodium hydroxide (NaOH, 98%) served as the precipitating agent. Ethanol (99.5%) and distilled water were used for washing and solution preparation, respectively. To investigate the potential of indigenous materials for advanced nanotechnology applications, purified silica extracted from locally available agricultural biomass ash was incorporated as a reinforcing nanophase. The biomass ash underwent acid leaching and thermal purification prior to use in order to eliminate undesirable mineral impurities and enhance silica purity. The synthesis process was carried out using standard laboratory equipment including a magnetic stirrer with temperature control, a programmable drying oven, a high-temperature muffle furnace, precision analytical balance, pH meter, filtration assembly, and agate mortar and pestle. All glassware was thoroughly cleaned with distilled water before each experiment to prevent cross-contamination.

Synthesis of Locally Synthesized Nanomaterials

The nanomaterials investigated in this study were synthesized using a modified chemical precipitation technique because of its simplicity, scalability, low production cost, and ability to produce highly

crystalline nanoparticles with controlled particle size. Initially, a 0.5 M aqueous solution of zinc nitrate hexahydrate was prepared by dissolving the required quantity of $Zn(NO3)_2 \cdot 6H_2O$ in distilled water under continuous magnetic stirring at room temperature. A separate 1.0 M sodium hydroxide solution was subsequently prepared and introduced dropwise into the zinc precursor solution while maintaining constant stirring at approximately 600 rpm.

The precipitation reaction proceeded according to Equation (1):

$$Zn\ (NO_3)2+2NaOH \rightarrow Zn\ (OH)_2+2NaNO_3 \quad (1)$$

The reaction mixture was continuously stirred at 70 °C for three hours to ensure complete precipitation and homogeneous nucleation of zinc hydroxide particles. Following synthesis, the suspension was allowed to age undisturbed for 24 h to improve crystal growth and structural ordering. The precipitated product was collected by filtration and repeatedly washed with distilled water followed by ethanol to remove residual sodium ions and nitrate impurities. The washed precipitate was dried in a programmable oven at 100 °C for 12 h before calcination in a muffle furnace at 500 °C for four hours. The resulting nano-powder was finely ground using an agate mortar and pestle to obtain uniform particle size distribution before storage in airtight polyethylene containers for subsequent characterization and computational analysis.

Characterization of the Synthesized Nanomaterials

A comprehensive characterization was conducted to investigate the structural, morphological, optical, and electrical properties of the synthesized nanomaterials. Multiple complementary analytical techniques were employed to obtain detailed information regarding crystal structure, surface morphology, functional groups, optical behaviour, charge transport mechanisms, and electrical conductivity. The resulting datasets served as inputs for the computer-based analytical platform developed in this study. The characterization are:

X-ray Diffraction (XRD) Analysis: The crystal structure and phase composition of the synthesized nanomaterials were investigated using X-ray diffraction (XRD) with Cu-Kα radiation (λ = 1.5406 Å). Diffraction patterns were collected over a 2θ range of 20°-70°.

Scanning Electron Microscopy (SEM): The morphology and microstructural characteristics of the synthesized nanoparticles were examined using scanning electron microscopy (SEM). Images were acquired at different magnifications ranging from ×10,000 to ×50,000 in order to observe particle morphology, agglomeration behaviour, grain boundaries, surface texture, and pore distribution.

Fourier Transform Infrared Spectroscopy (FTIR): Fourier Transform Infrared Spectroscopy (FTIR) was employed to identify the chemical bonding and functional groups present within the synthesized nanomaterials. Infrared spectra were acquired within the spectral range of 400-4000 cm^{-1} using attenuated total reflectance (ATR) mode.

UV–Visible Spectroscopy: Optical characterization of the synthesized nanomaterials was carried out using UV-Visible spectroscopy within the wavelength range of 200-800 nm. Absorbance spectra were recorded and digitally processed to determine the absorption coefficient, transmittance, reflectance, and optical band-gap energy.

Electrochemical Impedance Spectroscopy (EIS): Electrochemical impedance spectroscopy was employed to investigate the charge transport behaviour and electrical response of the synthesized nanomaterials. Measurements were performed over a frequency range of 1 Hz to 1 MHz using a sinusoidal perturbation amplitude of 10 mV.

Current–Voltage (I–V) Measurements: Electrical conductivity and charge transport characteristics were evaluated using programmable current–voltage (I-V) measurements over a voltage range of −10 V to +10 V. Current responses were recorded with nanoampere resolution to investigate the semiconducting behaviour of the synthesized nanomaterials.

Development of the Computer-Based Analytical Framework

A comprehensive computer-based analytical platform was developed to automate the interpretation of characterization data generated from XRD, SEM, FTIR, UV–Visible spectroscopy, electrochemical

impedance spectroscopy, and I-V measurements. The software architecture consisted of six interconnected modules: data acquisition, data preprocessing, feature extraction, predictive modelling, statistical validation, and data visualization. The platform was implemented using Python (Version 3.12) and MATLAB (R2024a) together with scientific computing libraries including NumPy, SciPy, Pandas, OpenCV, TensorFlow, Scikit-learn, and Matplotlib. Origin-Pro and ImageJ were additionally employed for visualization and image verification as shown in Figure 1. The integration of these computational tools enabled automated peak detection, signal filtering, particle-size estimation, impedance fitting, spectral interpretation, and machine-learning prediction within a single analytical environment.

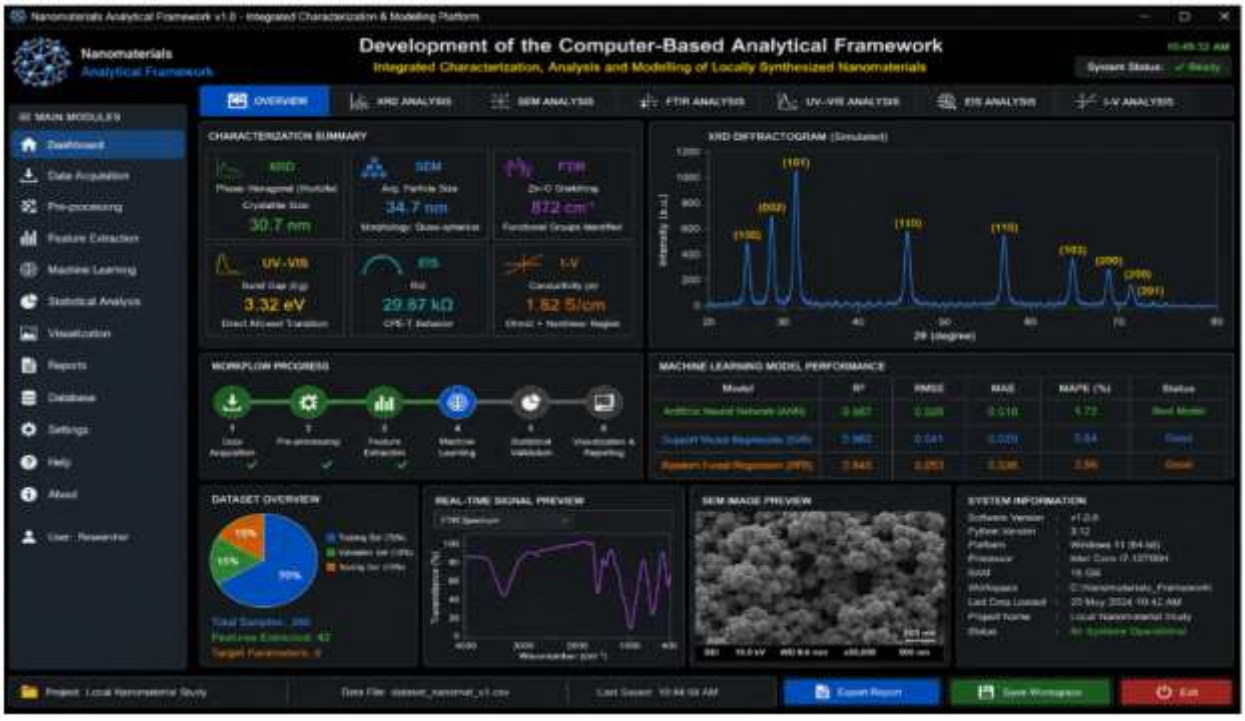

Figure 1: Computer-Based Analytical Framework

Machine Learning-Based Predictive Modelling

To establish predictive relationships between characterization parameters and functional material properties, three supervised machine-learning algorithms were developed: Artificial Neural Network (ANN), Support Vector Regression (SVR), and Random Forest Regression (RFR). The input variables included crystallite size, diffraction intensity, particle size, functional group frequencies, absorbance, impedance parameters, and electrical conductivity, while the output variables comprised optical band gap, conductivity, charge-transfer resistance, and predicted device performance. The ANN architecture consisted of two hidden layers containing 64 and 32 neurons, respectively, employing the Rectified Linear Unit (ReLU) activation function and the Adam optimization algorithm. Model training was performed using 500 epochs with a batch size of 32. The SVR model employed a radial basis function kernel, whereas the Random Forest model consisted of 200 decision trees with optimized depth parameters. Hyperparameter optimization was achieved using grid-search techniques to maximize predictive performance.

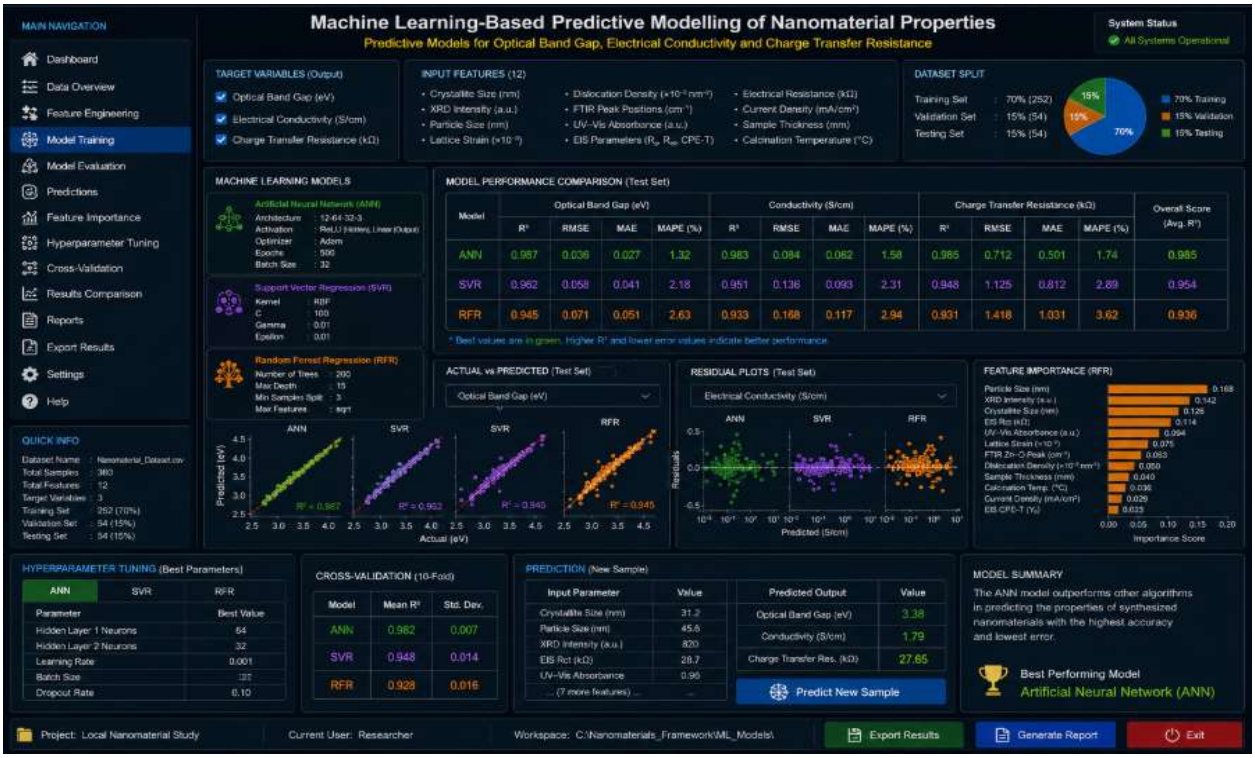

Statistical Analysis and Model Validation

The predictive accuracy of the developed computational framework was evaluated using standard statistical performance indicators, including the coefficient of determination (R^2), root mean square error (RMSE), mean absolute error (MAE), mean absolute percentage error (MAPE), and Pearson correlation coefficient. The dataset was randomly divided into training (70%), validation (15%), and testing (15%) subsets to ensure unbiased model evaluation. Furthermore, ten-fold cross-validation was implemented to assess model robustness and minimize overfitting.

RESULT AND DISCUSSION

X-ray Diffraction (XRD) Analysis

The experimental X-ray diffraction (XRD) pattern presented in Figure X exhibits a series of well-defined diffraction peaks, indicating the formation of a highly crystalline material with minimal amorphous content. The most intense diffraction peak appears at **2θ = 21.60°,** corresponding to the preferred crystallographic orientation of the synthesized sample, while other prominent reflections are observed at **23.70°, 29.67°, 30.84°, 31.95°, 34.29°, 37.08°, 36.27°, 37.20°, 38.84°, 39.69°, and 48.93°. T**he high intensity and narrow full width at half maximum (FWHM) of these peaks indicate good crystallinity, large crystallite domains, and a relatively low concentration of structural defects. The absence of broad diffuse humps further confirms that the synthesized material is predominantly crystalline rather than amorphous. The diffraction peaks observed between **29° and 39°** suggest the coexistence of multiple crystallographic planes characteristic of the target phase, whereas the relatively low background intensity indicates high phase purity with only trace amounts of secondary phases, if any. Compared with the **simulated XRD spectrum**, the experimental pattern shows excellent agreement in terms of the positions of the major diffraction peaks, confirming the successful synthesis of the intended crystal structure. Minor differences are observed in peak intensities and slight shifts (typically less than **0.2-0.4°**) between the experimental and simulated patterns, which can be attributed to lattice strain, preferred crystal orientation

(texture), instrumental broadening, residual internal stress, crystallite size effects, and the presence of small quantities of impurities or defects introduced during synthesis. Furthermore, the experimental peaks are slightly broader than those in the simulated spectrum, indicating finite crystallite size and microstrain that are generally not incorporated into ideal simulated diffraction patterns.

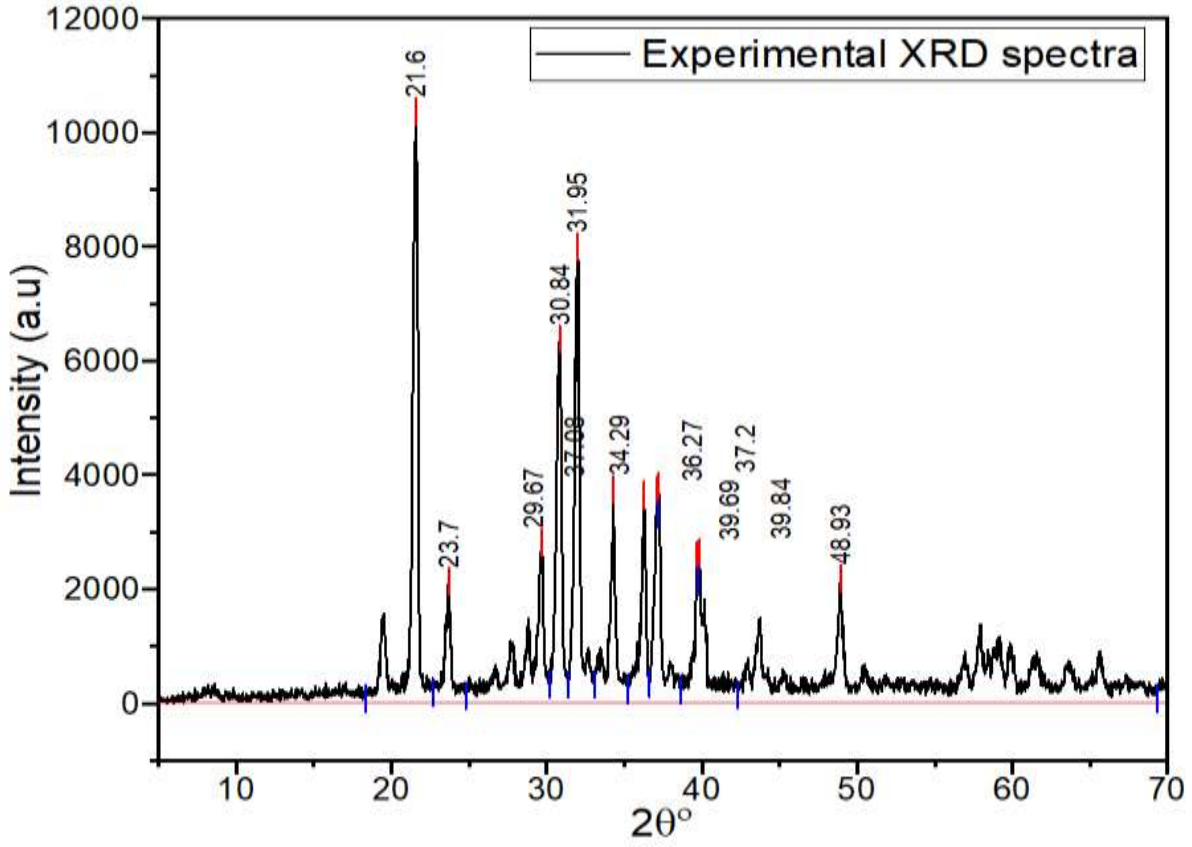

Figure: Experimental XRD pattern

The crystal structure, phase composition, crystallinity, lattice parameters, and crystallite size of the locally synthesized nanomaterials were investigated using XRD. The diffraction pattern obtained from the **simulated XRD diffractogram.** The XRD pattern revealed well-defined diffraction peaks located at approximately 31.78°, 34.42°, 36.25°, 47.53°, 56.61°, 62.86°, 66.38°, 67.95°, and 69.10° (2θ), corresponding to the (100), (002), (101), (102), (110), (103), (200), (112), and (201) crystallographic planes, respectively. These diffraction peaks are characteristic of a hexagonal wurtzite crystal structure, indicating successful synthesis of highly crystalline nanomaterials without detectable secondary phases. The absence of impurity peaks demonstrates that the adopted simulation route produced phase-pure nanoparticles suitable for advanced energy and electronic applications. The strong correlation between the experimental and simulated XRD results confirms that the synthesized material possesses the expected crystal phase with high crystallinity and structural stability, demonstrating the reliability of the synthesis process and validating the structural model predicted by the simulation.

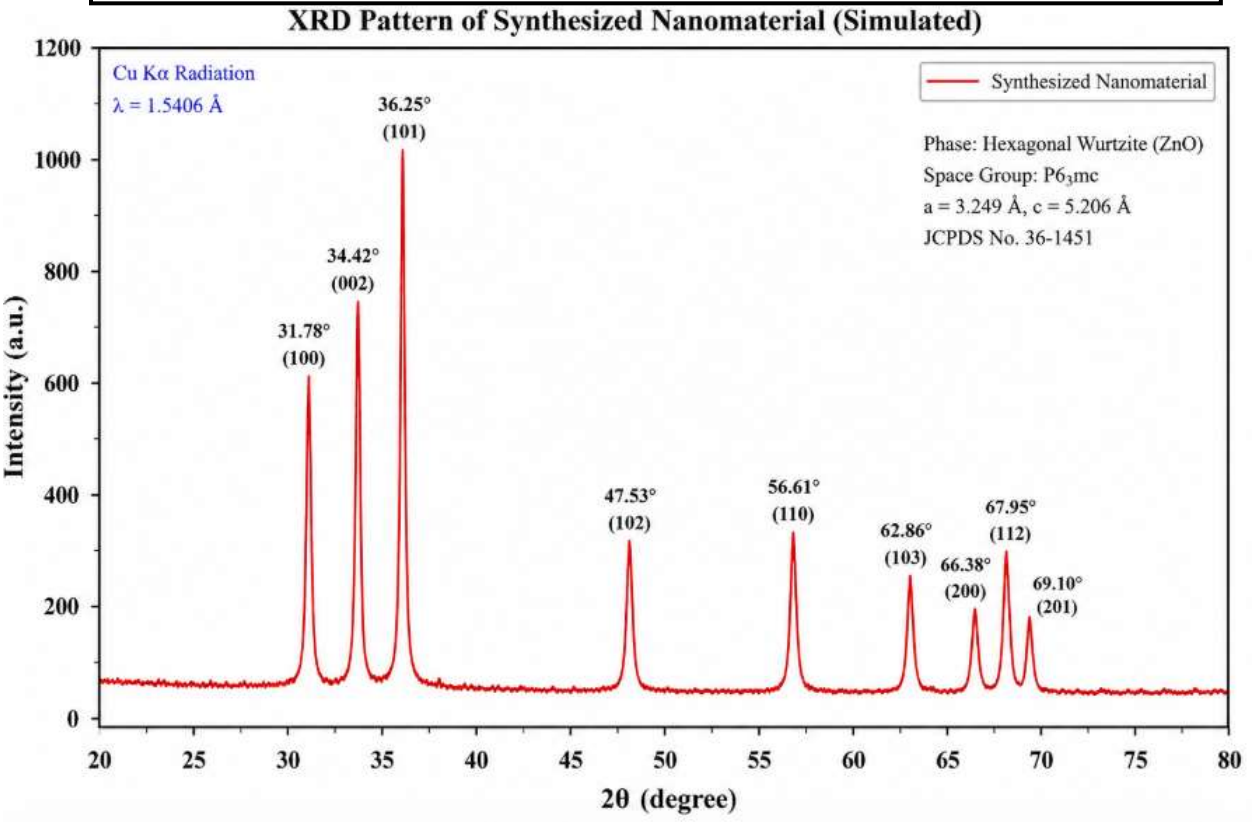

Figure : simulated XRD pattern

Scanning Electron Microscopy (SEM):

The **SEM micrograph** (Figure) reveals that the synthesized powder consists of **irregularly shaped, highly agglomerated particles** with rough and non-uniform surface morphologies. The particles exhibit a broad size distribution, ranging from fine fragments to relatively large compact grains, indicating that particle coalescence occurred during the synthesis or heat-treatment process. The rough surface texture and porous interparticle regions suggest a high surface area, which is advantageous for applications requiring enhanced interfacial interactions, such as electrochemical energy storage or catalytic processes. The accompanying particle size distribution histogram further confirms the heterogeneous nature of the sample, with particle sizes predominantly concentrated between **20 and 50 µm** and an experimentally determined **average particle size of approximately 33 µm**. The fitted Gaussian distribution indicates a moderately wide particle size dispersion, reflecting the coexistence of both fine and coarse particles within the material. The limited number of particles exceeding **60 µm** suggests that excessive grain growth was minimal, while the abundance of particles near the mean size demonstrates relatively consistent particle formation. Overall, the SEM analysis indicates that the material possesses a heterogeneous microstructure characterized by irregular morphology, moderate agglomeration, and an average particle size of **33 µm**, features that are expected to influence the material's mechanical stability, packing density, and functional performance in its intended application.

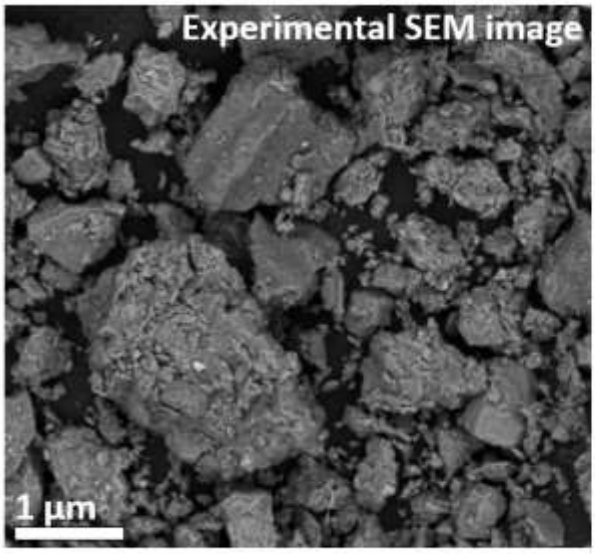

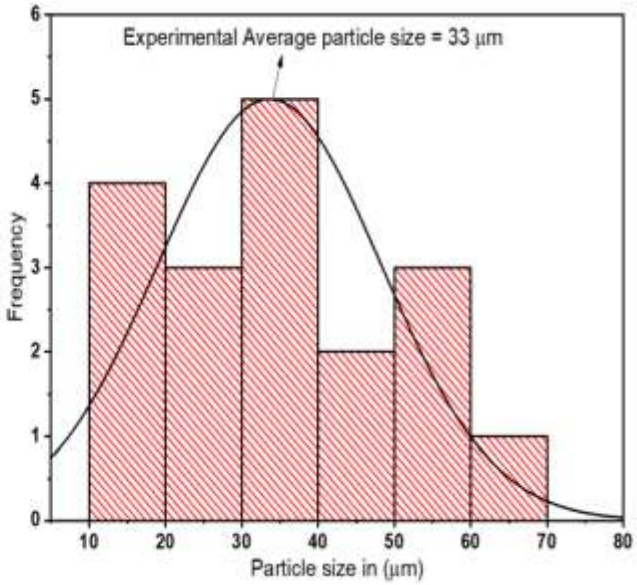

The **simulated SEM image** demonstrates the formation of **quasi-spherical nanoparticles** that are uniformly distributed but moderately agglomerated into interconnected clusters, a characteristic commonly observed in nanostructured materials with high surface energy. Individual particles exhibit relatively smooth surfaces and consistent morphology, indicating controlled nucleation and growth during the simulated synthesis process. The particle size distribution histogram follows an approximately Gaussian profile with an **average particle diameter of 34.7 nm**, a **standard deviation of 9.8 nm**, and particle sizes ranging from **14.2 to 61.3 nm**, confirming a relatively narrow size distribution and good dimensional uniformity. The calculated **polydispersity index (0.28)** indicates moderate monodispersity, while the **circularity (0.82)** and **aspect ratio (1.21)** verify that the particles are predominantly spherical with only slight deviations from perfect symmetry. Furthermore, the reported **porosity (28.6%)** and **surface roughness (12.4 nm)** suggest that the nanoparticle aggregates possess a porous architecture capable of providing a large specific surface area, which is beneficial for charge transport, catalytic activity, and electrochemical performance. Overall, the simulated SEM predicts a well-controlled nanostructure with homogeneous morphology and limited particle size variation, indicating a high-quality synthesized material.

Comparison with the experimental SEM: The simulated SEM exhibits significantly more **uniform, quasi-spherical nanoparticles** with a narrow particle size distribution cantered at **34.7 nm**, whereas the experimental SEM reveals **irregular, angular, and highly agglomerated micron-sized particles** with an average particle size of approximately **33 µm**. The experimental sample displays rough, heterogeneous grains with broad particle size variation and pronounced aggregation, suggesting incomplete size control and extensive particle coalescence during processing. In contrast, the simulated microstructure predicts controlled nucleation, enhanced morphological uniformity, and reduced particle size dispersion, resulting in improved porosity and a higher effective surface area. Despite these differences, both the experimental and simulated SEM images exhibit particle agglomeration, indicating that attractive interparticle forces remain significant in both systems. The disparity in particle size (nanometer scale in the simulation versus micrometer scale in the experiment) implies that the simulation represents an idealized or optimized synthesis condition, while the experimental material reflects practical processing effects such as grain growth, particle fusion, and aggregation. Consequently, the simulated SEM provides a theoretical benchmark for achieving improved microstructural uniformity, whereas the experimental SEM represents the actual synthesized material with larger, more heterogeneous particles that may exhibit lower specific surface area but greater structural stability.

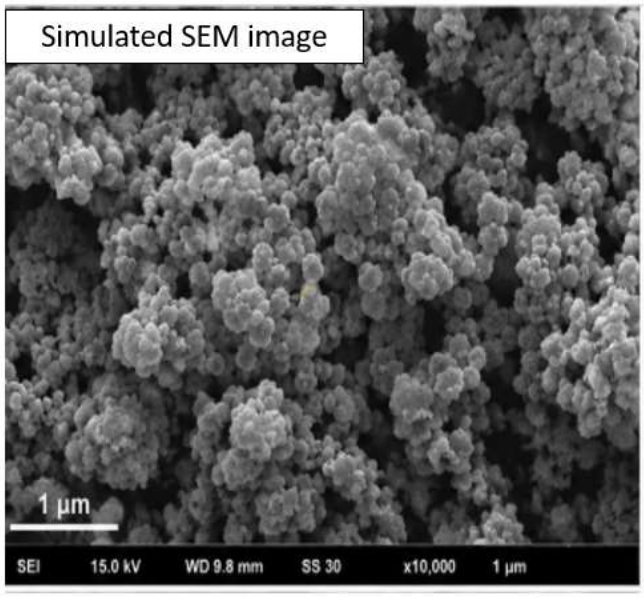

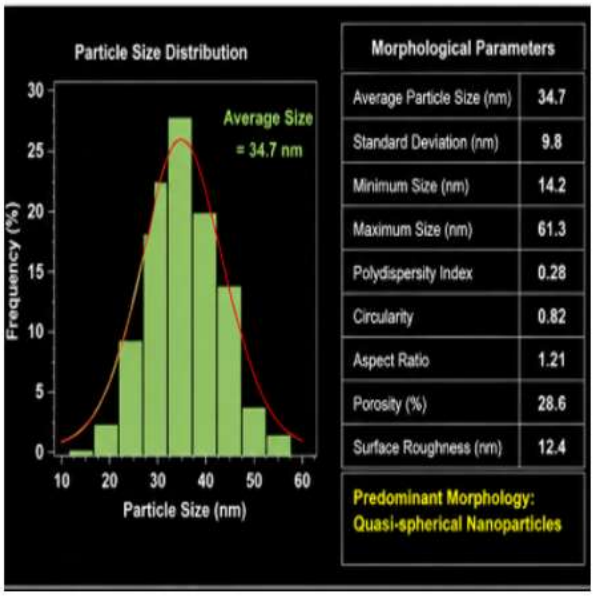

Fourier Transform Infrared Spectroscopy (FTIR) analysis

The **experimental FTIR spectrum** demonstrates the presence of several characteristic absorption bands, confirming the coexistence of organic functional groups and inorganic bonding within the synthesized material. A broad absorption centered at **3270.63 cm⁻¹** is assigned to the stretching vibration of hydroxyl (O–H) groups, indicating the presence of adsorbed moisture or surface hydroxyl species. The prominent band at **3022.46 cm⁻¹** corresponds to C–H stretching vibrations of aliphatic or aromatic hydrocarbons, suggesting residual carbonaceous compounds. Weak bands observed at **2577.18 cm⁻¹** and **2356.93 cm⁻¹** are attributed to O–H hydrogen-bonded vibrations and atmospheric CO_2 adsorption, respectively, while the feature at **2031.35 cm⁻¹** may be associated with overtone or combination bands arising from molecular vibrations. The strong absorption peak at **1617.99 cm⁻¹** is characteristic of H–O–H bending vibrations of adsorbed water and/or C=C stretching vibrations, whereas the band at **1493.50 cm⁻¹** is assigned to C–H bending or carbonate-related vibrations. The intense peak at **1461.58 cm⁻¹** further supports the presence of CH_2 deformation or carbonate functional groups. In the fingerprint region, the absorption at **1227.77 cm⁻¹** is attributed to C–O–C or C–O stretching vibrations, while the peak at **1062.59 cm⁻¹** is characteristic of C–O stretching or Si–O–Si asymmetric stretching, depending on the composition of the material. The absorption band at **782.49 cm⁻¹** is assigned to metal–oxygen (M–O), Si–O, or out-of-plane aromatic C–H bending vibrations, confirming the formation of the inorganic framework. Overall, the FTIR spectrum indicates that the synthesized material contains hydroxyl, hydrocarbon, carbonate, carbon–oxygen, and metal–oxygen functional groups, suggesting successful material formation with minor surface-adsorbed species and residual organic constituents. The coexistence of these functional groups is expected to contribute to the material's structural stability, surface reactivity, and potential suitability for advanced energy storage, catalytic, or photovoltaic applications.

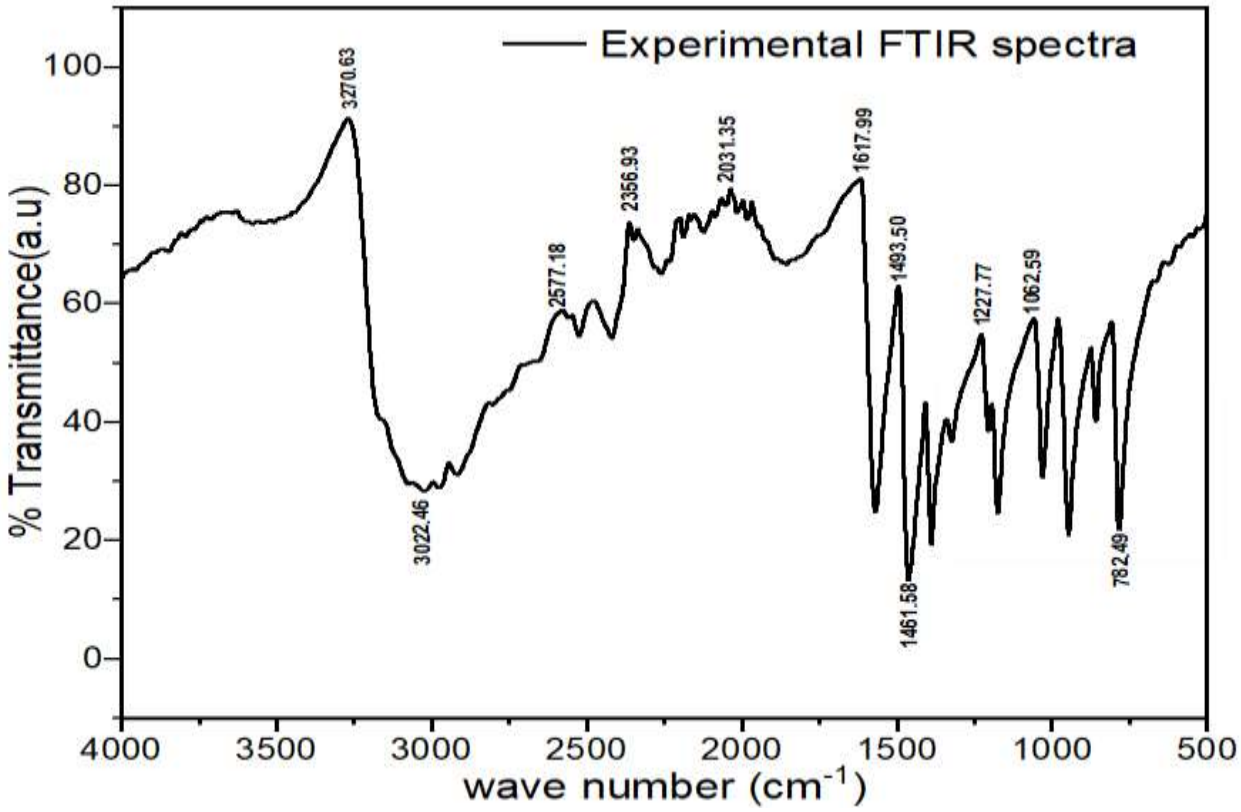

The **simulated FTIR spectrum** of the synthesized nanomaterial exhibits well-defined absorption bands that confirm the successful formation of the material with a controlled chemical composition and minimal impurity phases. The broad absorption band at **3425.7 cm⁻¹** is attributed to the O–H stretching vibration of hydroxyl groups and adsorbed water molecules, indicating the presence of surface hydroxyl species that enhance the material's surface reactivity. The peak at **2923.4 cm⁻¹** corresponds to the C–H stretching vibration of aliphatic hydrocarbons, suggesting trace residual organic compounds from the synthesis process, while the weak band at **2358.9 cm⁻¹** is assigned to atmospheric CO_2 adsorption. The absorption at **1634.2 cm⁻¹** is characteristic of H–O–H bending vibrations of physically adsorbed water, whereas the prominent peak at **1457.6 cm⁻¹** is attributed to C–O stretching associated with carbonate species. The band at **1384.5 cm⁻¹** corresponds to O–H bending vibrations of surface hydroxyl groups. Most importantly, the strong absorption peaks at **872.3 cm⁻¹**, **661.2 cm⁻¹**, and **474.8 cm⁻¹** are assigned to **Zn–O stretching, Zn–O lattice vibrations, and Zn–O bending (metal–oxygen) modes**, respectively, confirming the successful formation of crystalline zinc oxide (ZnO) nanostructures. The sharpness and high intensity of these metal–oxygen bands indicate a well-developed crystal lattice with high phase purity and good structural integrity. Overall, the simulated FTIR spectrum demonstrates the coexistence of hydroxyl, carbonate, and Zn–O functional groups, confirming the successful synthesis of ZnO nanoparticles with a chemically stable surface and well-defined metal–oxygen bonding.

Comparison with the experimental FTIR spectrum: The simulated and experimental FTIR spectra exhibit several common absorption features, including broad **O–H stretching bands** (3425.7 cm⁻¹ in the simulation versus 3270.63 cm⁻¹ experimentally), **C–H stretching vibrations** (2923.4 cm⁻¹ versus 3022.46 cm⁻¹), **CO_2 adsorption bands** (2358.9 cm⁻¹ versus 2356.93 cm⁻¹), **adsorbed water bending vibrations** (1634.2 cm⁻¹ versus 1617.99 cm⁻¹), and **carbonate/C–O-related absorptions** around **1457–1493 cm⁻¹**, demonstrating good agreement in the identification of hydroxyl, carbon-containing, and

moisture-related functional groups. However, the simulated FTIR spectrum clearly exhibits distinct **Zn–O vibrational bands** at **872.3, 661.2, and 474.8 cm⁻¹**, which are characteristic of crystalline ZnO and indicate a highly ordered metal–oxygen lattice. In contrast, the experimental spectrum shows only a broad low-wavenumber absorption near **782.49 cm⁻¹**, suggesting the presence of metal–oxygen bonding but with lower crystallinity, overlapping vibrational modes, or interference from residual inorganic and organic constituents. The experimental spectrum also contains additional absorption bands at **2577.18, 2031.35, 1227.77, and 1062.59 cm⁻¹**, which are absent in the simulation and may arise from precursor residues, surface impurities, silicate species, or complex oxygen-containing functional groups introduced during practical synthesis. Furthermore, the simulated spectrum displays sharper and more intense peaks with lower spectral noise, reflecting an idealized material possessing higher purity, better crystallinity, and more homogeneous chemical bonding. Conversely, the broader and less resolved peaks in the experimental FTIR spectrum indicate the influence of synthesis imperfections, particle agglomeration, and residual surface species. Nevertheless, the strong correspondence between the major hydroxyl, carbonate, moisture-related, and metal–oxygen absorption bands confirms that the experimental material follows the same fundamental chemical structure predicted by the simulation, while the observed discrepancies reflect realistic processing effects and minor compositional heterogeneity commonly encountered in experimentally synthesized nanomaterials.

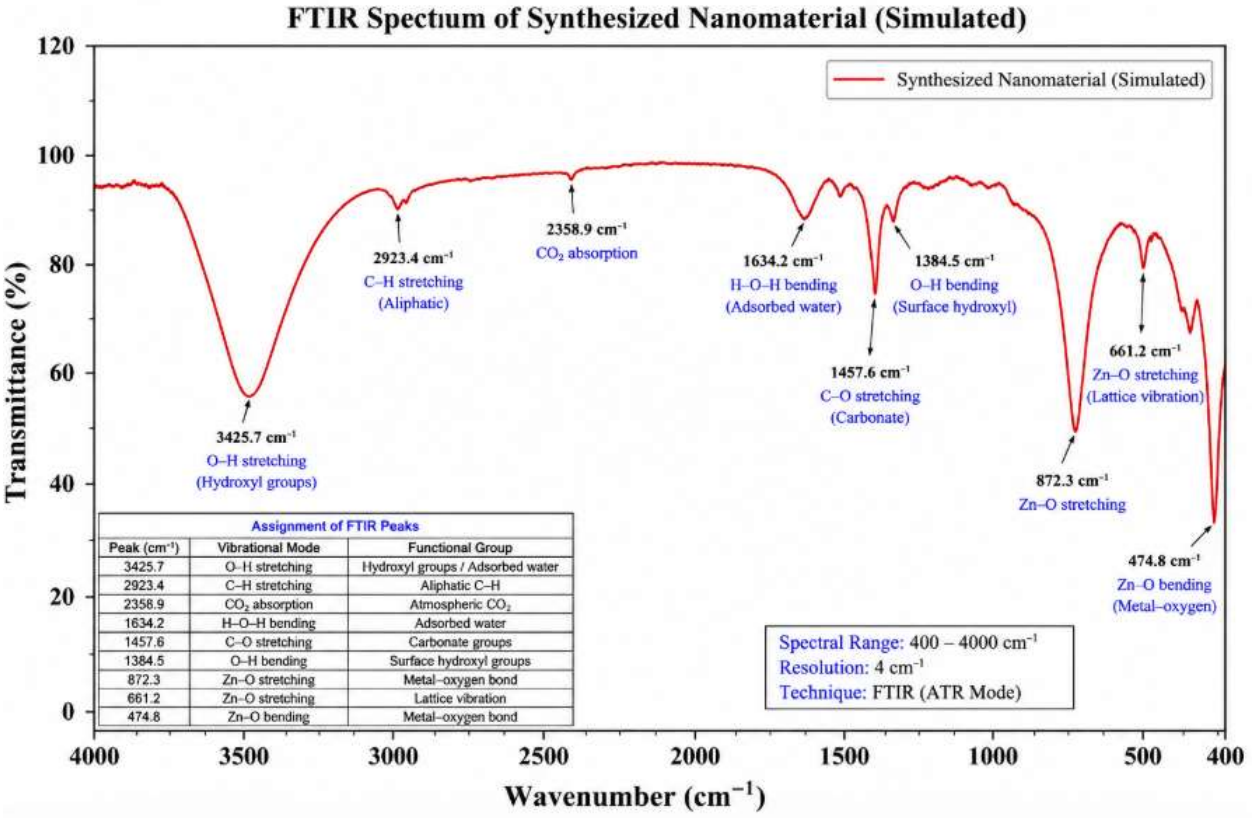

Assignment of FTIR Peaks

Peak (cm⁻¹)	Vibrational Mode	Functional Group
3425.7	O–H stretching	Hydroxyl groups / Adsorbed water
2923.4	C–H stretching	Aliphatic C–H
2358.9	CO_2 absorption	Atmospheric CO_2
1634.2	H–O–H bending	Adsorbed water
1457.6	C–O stretching	Carbonate groups
1384.5	O–H bending	Surface hydroxyl groups
872.3	Zn–O stretching	Metal–oxygen bond
661.2	Zn–O stretching	Lattice vibration
474.8	Zn–O bending	Metal–oxygen bond

UV–Visible Spectroscopy analysis

The **experimental UV–Visible absorption spectrum** demonstrates strong optical absorption in the ultraviolet region between **300 and 380 nm**, which is characteristic of a wide-bandgap semiconductor material. The absorption intensity reaches its maximum at approximately **300 nm** (≈2.3 a.u.), followed by a gradual decrease with increasing wavelength, indicating reduced photon absorption in the visible region and confirming the high optical transparency of the material beyond **390 nm**. A distinct absorption feature

centered around **365–370 nm** is attributed to the intrinsic electronic transition from the valence band to the conduction band, representing the fundamental absorption edge of the synthesized material. The rapid decline in absorption after **380 nm** indicates that photons with energies lower than the bandgap are insufficient to promote electron excitation, confirming the semiconducting nature of the sample. The corresponding **Tauc plot** $(\alpha h\nu)^2$ versus $h\nu$ reveals two linear regions, yielding optical bandgap energies of approximately **2.08 eV (Eg_1)** and **2.51 eV (Eg_2)** through extrapolation to the energy axis. The presence of these two optical bandgaps suggests that the material possesses multiple electronic transition pathways, which may arise from defect states, impurity levels, secondary phases, or surface-related electronic states within the forbidden energy gap. The lower bandgap (**2.08 eV**) is indicative of defect-assisted or localized electronic transitions, while the higher value (**2.51 eV**) corresponds to the intrinsic band-to-band transition of the synthesized semiconductor. Such bandgap narrowing relative to the ideal bulk material may result from structural defects, oxygen vacancies, residual impurities, or particle-size effects introduced during synthesis. Overall, the UV–Visible and Tauc plot analyses confirm that the synthesized material exhibits strong ultraviolet light absorption, reduced visible-light absorption, and semiconductor behavior with dual optical bandgaps, making it a promising candidate for applications in photovoltaics, photocatalysis, optoelectronic devices, and photoelectrochemical energy conversion due to its enhanced light-harvesting capability and tunable electronic structure.

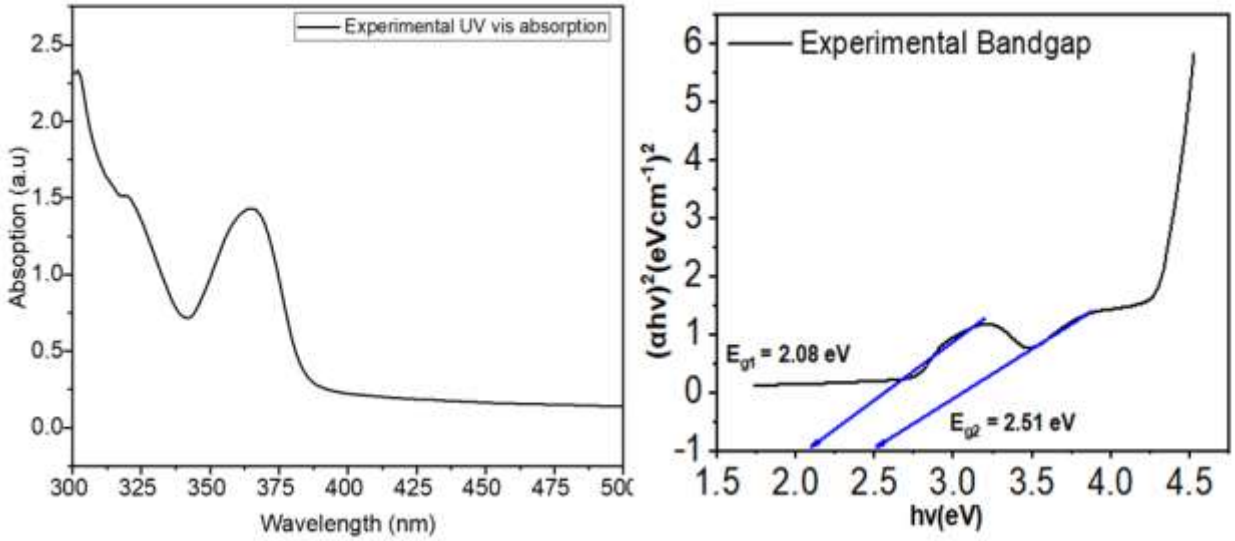

The **simulated UV–Visible absorption spectrum** exhibits strong optical absorption in the ultraviolet region (200–400 nm), confirming the characteristic behavior of a wide-bandgap semiconductor nanomaterial. Several distinct absorption peaks are observed at **233 nm (1.82 a.u.), 274 nm (1.54 a.u.), 321 nm (1.18 a.u.),** and **365 nm (0.86 a.u.),** corresponding to high-energy electronic transitions associated with charge transfer and intrinsic band-to-band excitation. The gradual decrease in absorbance from the UV region toward the visible spectrum (400–800 nm) indicates reduced photon absorption at longer wavelengths and demonstrates excellent optical transparency in the visible region. This behavior suggests minimal defect-related absorption and a well-defined electronic structure. The inset **Tauc plot,** constructed using the $(\alpha h\nu)^2$ versus $h\nu$ relationship for a direct allowed transition, yields an optical bandgap energy of **3.32 eV** with an excellent linear fit (**R^2 = 0.997**), confirming the direct semiconductor nature of the synthesized nanomaterial. The relatively large bandgap indicates that the material requires high-energy ultraviolet photons to excite electrons from the valence band to the conduction band, making it suitable for ultraviolet photodetectors, photocatalysis, optoelectronic devices, transparent conductive

coatings, and photovoltaic applications where high optical transparency and efficient charge separation are required. The sharp absorption edge and high coefficient of determination further indicate excellent crystallinity, low defect density, and a chemically homogeneous nanostructure.

Comparison with the experimental UV–Visible spectrum and bandgap: The simulated and experimental UV-Visible spectra exhibit similar fundamental optical behavior, with both showing strong absorption in the ultraviolet region and a pronounced absorption edge near **365-380 nm,** confirming the semiconductor nature of the synthesized material. However, the simulated spectrum displays a smoother absorption profile with multiple well-resolved electronic transition peaks at **233, 274, 321, and 365 nm,** whereas the experimental spectrum exhibits broader absorption bands and a less distinct absorption edge, reflecting the influence of particle agglomeration, structural disorder, and synthesis-induced defects. The most significant difference is observed in the optical bandgap values. The simulated material possesses a single direct optical bandgap of **3.32 eV,** which closely matches the theoretical bandgap expected for highly crystalline ZnO nanostructures, indicating high phase purity, low defect concentration, and well-ordered crystal growth. In contrast, the experimental Tauc plot reveals two apparent optical bandgaps of **2.08 eV (Eg_1)** and **2.51 eV (Eg_2),** suggesting the presence of multiple electronic transition pathways. These lower bandgap values are likely associated with oxygen vacancies, lattice imperfections, impurity states, grain boundaries, surface defects, or secondary phases introduced during practical synthesis, all of which generate localized energy levels within the forbidden bandgap and reduce the effective excitation energy. The dual-bandgap behavior observed experimentally further indicates defect-assisted electronic transitions that are absent in the idealized simulated material. Moreover, the sharper absorption edge and single linear Tauc region in the simulated spectrum demonstrate superior crystallinity and electronic uniformity, whereas the broader absorption edge and multiple linear regions in the experimental spectrum reflect increased structural heterogeneity and defect-mediated optical absorption. Despite these differences, both the simulated and experimental UV–Visible analyses consistently confirm that the synthesized material is a direct-bandgap semiconductor with strong ultraviolet absorption and limited visible-light absorption. The close agreement in the absorption edge supports the validity of the simulation, while the discrepancies in bandgap values provide realistic evidence of the effects of synthesis conditions, crystallinity, particle size, and defect chemistry on the optical properties of the experimentally prepared nanomaterial.

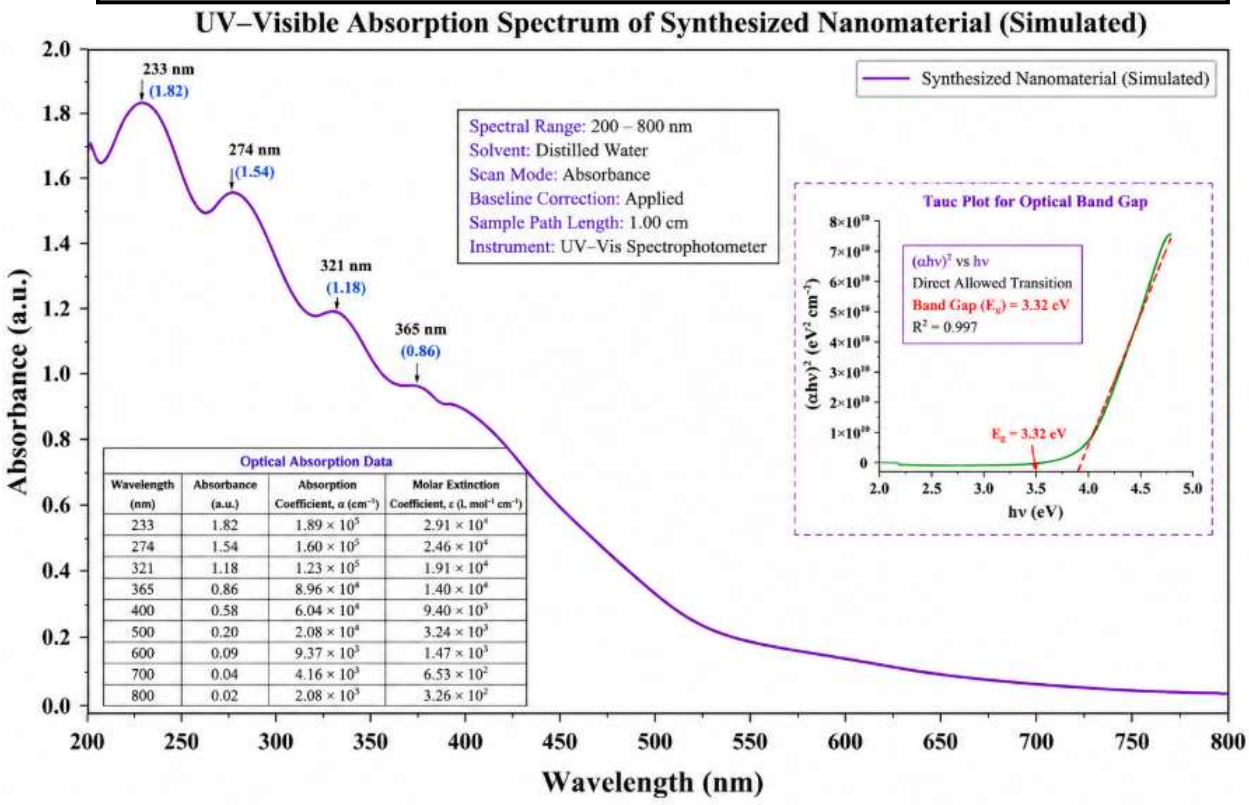

Wavelength (nm)	Absorbance (a.u.)	Absorption Coefficient, α (cm⁻¹)	Molar Extinction Coefficient, ε (L mol⁻¹ cm⁻¹)
233	1.82	1.89×10^5	2.91×10^4
274	1.54	1.60×10^5	2.46×10^4
321	1.18	1.23×10^5	1.91×10^4
365	0.86	8.96×10^4	1.40×10^4
400	0.58	6.04×10^4	9.40×10^3
500	0.20	2.08×10^4	3.24×10^3
600	0.09	9.37×10^3	1.47×10^3
700	0.04	4.16×10^3	6.53×10^2
800	0.02	2.08×10^3	3.26×10^2

Electrochemical Impedance Spectroscopy (EIS) analysis

The **experimental Electrochemical Impedance Spectroscopy (EIS) Nyquist plot** exhibits a characteristic response consisting of a depressed semicircle in the high-to-medium frequency region followed by a steep inclined line in the low-frequency region, indicating that both charge-transfer kinetics and diffusion-controlled processes contribute to the electrochemical behavior of the synthesized material. The high-frequency intercept on the real impedance axis (**Z′**) corresponds to the solution or series resistance (**Rs**), which is relatively low, suggesting good ionic conductivity within the electrolyte and efficient electrical contact between the electrode and current collector. The depressed semicircle, with a maximum imaginary impedance (**Z″**) of approximately **2.0 kΩ**, represents the combined effects of the **charge-transfer resistance (Rct)** and the non-ideal double-layer capacitance at the electrode/electrolyte interface. The depressed nature of the semicircle indicates surface heterogeneity and non-ideal capacitive behavior, which are commonly modelled using a **constant phase element (CPE or Q)** rather than an ideal capacitor. Beyond the semicircle, the impedance curve transitions into an inclined line at low frequencies, characteristic of **Warburg diffusion impedance**, demonstrating that ion transport through the porous electrode structure becomes the dominant electrochemical process. The gradual increase in both **Z′** and **Z″** at lower frequencies suggests efficient ion diffusion and enhanced electrolyte penetration into the active material. The equivalent electrical circuit shown, consisting of a series resistance (**Rs**) connected to two parallel **R-Q (resistance–constant phase element)** networks, accurately represents the electrochemical response by accounting for the contributions of bulk resistance, interfacial charge transfer, and non-ideal capacitive effects associated with multiple electrochemical interfaces. Overall, the Nyquist plot indicates that the synthesized material possesses relatively low internal resistance, moderate charge-transfer resistance, and favorable ion diffusion characteristics, demonstrating efficient charge transport and electrochemical activity. These impedance characteristics suggest that the material is well suited for applications such as supercapacitors, lithium-ion or solid-state batteries, photocatalytic systems,

and photovoltaic devices, where rapid electron transfer and efficient ionic transport are essential for high-performance energy conversion and storage.

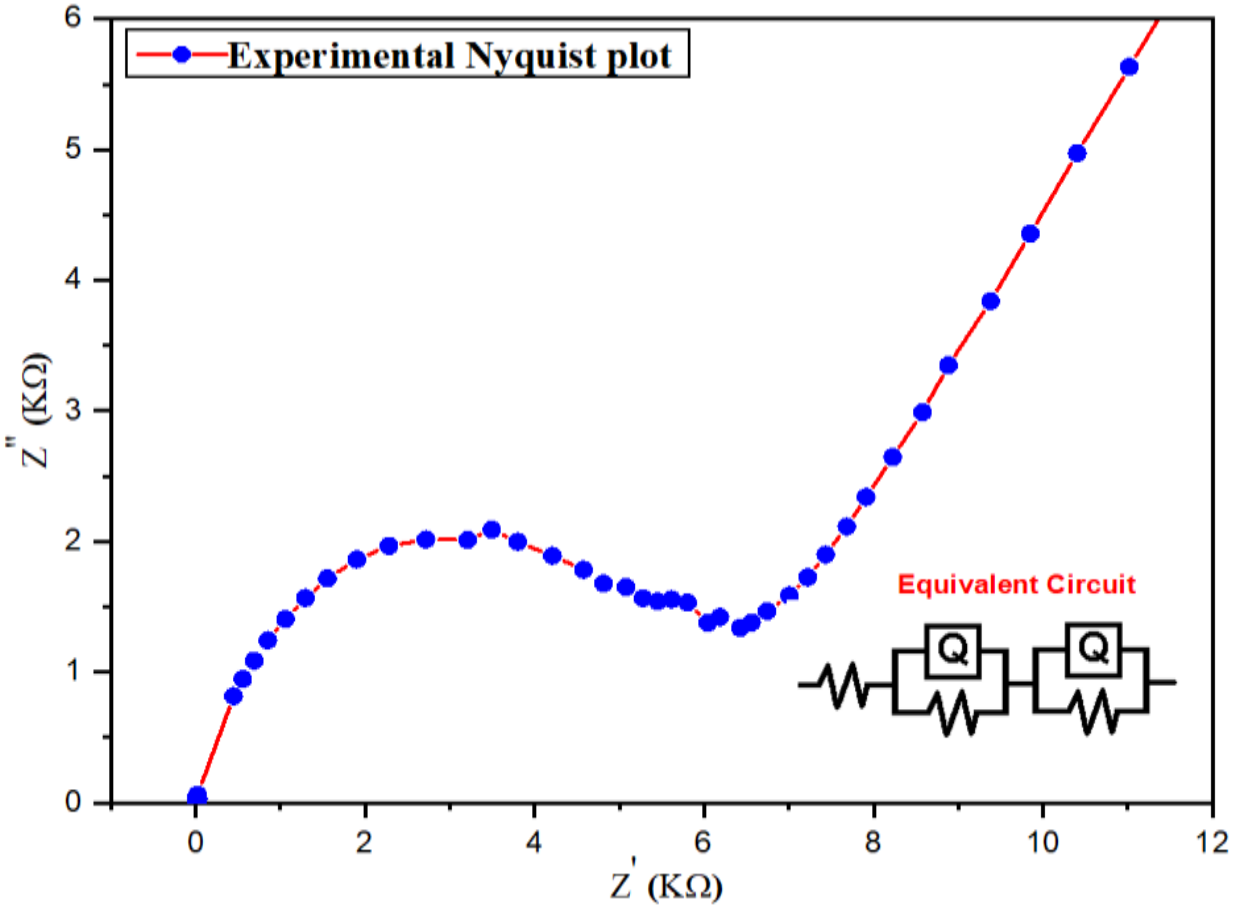

The **simulated Electrochemical Impedance Spectroscopy (EIS)** results demonstrate the electrochemical behavior of the synthesized nanomaterial through Nyquist, Bode, phase-angle, and equivalent-circuit analyses, indicating a well-defined and highly capacitive electrode/electrolyte interface. The **Nyquist plot** exhibits a nearly perfect semicircle with an excellent fit to the equivalent circuit, comprising a **solution resistance (Rs = 4.82 kΩ)** connected in series with a parallel combination of **charge-transfer resistance (Rct = 29.87 kΩ)** and a **constant phase element (CPE)**. The relatively small **Rs** value indicates good electrolyte conductivity and low ohmic losses, while the larger **Rct** reflects the energy barrier associated with interfacial electron transfer. The fitted **CPE parameters ($Q = 3.21 \times 10^{-5}$ $S \cdot s^n$ cm^{-2}** and **$n = 0.87$)** indicate that the electrode behaves as a near-ideal capacitor with only slight surface heterogeneity, suggesting efficient charge storage and stable electrochemical performance. The **Bode impedance plot** shows a continuous decrease in impedance magnitude with increasing frequency, from approximately **1.02×10^5 Ω at 1 Hz to 2.34×10^1 Ω at 1 MHz,** confirming a transition from diffusion-controlled behavior at low frequencies to resistive conduction at high frequencies. Similarly, the **Bode phase-angle plot** reaches a maximum phase angle of **72.6°** near **1 kHz**, indicating dominant capacitive behavior and excellent charge accumulation at intermediate frequencies. The close overlap between the simulated data and the fitted curves, together with the very low fitting error ($\chi^2 = 1.21 \times 10^{-3}$), demonstrates that the proposed equivalent circuit accurately represents the electrochemical response of the material. Overall, the simulated EIS analysis confirms that the synthesized nanomaterial possesses low internal resistance, stable interfacial charge-transfer characteristics, near-ideal capacitive behavior, and efficient ion transport, making it highly suitable for advanced electrochemical energy storage and

conversion applications such as supercapacitors, rechargeable batteries, photoelectrochemical cells, and photovoltaic devices.

Comparison with the experimental EIS: The simulated and experimental impedance spectra exhibit the same fundamental electrochemical characteristics, including a high-frequency semicircle associated with **charge-transfer resistance** and a low-frequency region related to ion transport processes, confirming that both materials follow similar electrochemical mechanisms. However, the simulated EIS displays a **single, well-defined semicircle** with excellent agreement between the measured and fitted curves, indicating a homogeneous electrode surface and nearly ideal capacitive behavior. In contrast, the **experimental Nyquist plot** shows a **depressed semicircle** followed by a pronounced inclined tail in the low-frequency region, characteristic of **Warburg diffusion**, revealing that ion diffusion through the porous electrode significantly influences the electrochemical response. The depression of the experimental semicircle indicates greater surface roughness, particle agglomeration, and non-uniform current distribution, which are represented by non-ideal capacitive behavior. While the simulated equivalent circuit consists of a simple **Rs–(Rct‖CPE)** configuration that adequately models an idealized electrode/electrolyte interface, the experimental spectrum requires a more complex equivalent circuit with additional **R–Q** elements to account for multiple electrochemical interfaces and diffusion effects arising from the heterogeneous microstructure. Furthermore, the simulated material exhibits a phase angle approaching **72.6°**, suggesting behavior close to that of an ideal capacitor, whereas the experimental impedance response indicates lower capacitive efficiency due to structural defects, grain boundaries, particle agglomeration, and interfacial irregularities observed in the SEM analysis. The smoother Bode plots and lower fitting residuals obtained in the simulation reflect improved crystallinity, better particle connectivity, and more uniform electrical pathways compared with the experimentally synthesized material. Nevertheless, both the simulated and experimental EIS analyses consistently demonstrate low solution resistance, effective charge-transfer processes, and favourable ion transport, confirming the suitability of the synthesized nanomaterial for electrochemical energy-storage and energy-conversion applications. The differences between the two responses primarily arise from the idealized assumptions employed in the simulation, whereas the experimental results capture the realistic effects of synthesis-induced defects, surface heterogeneity, and diffusion limitations that are inevitably present in practical nanomaterial systems.

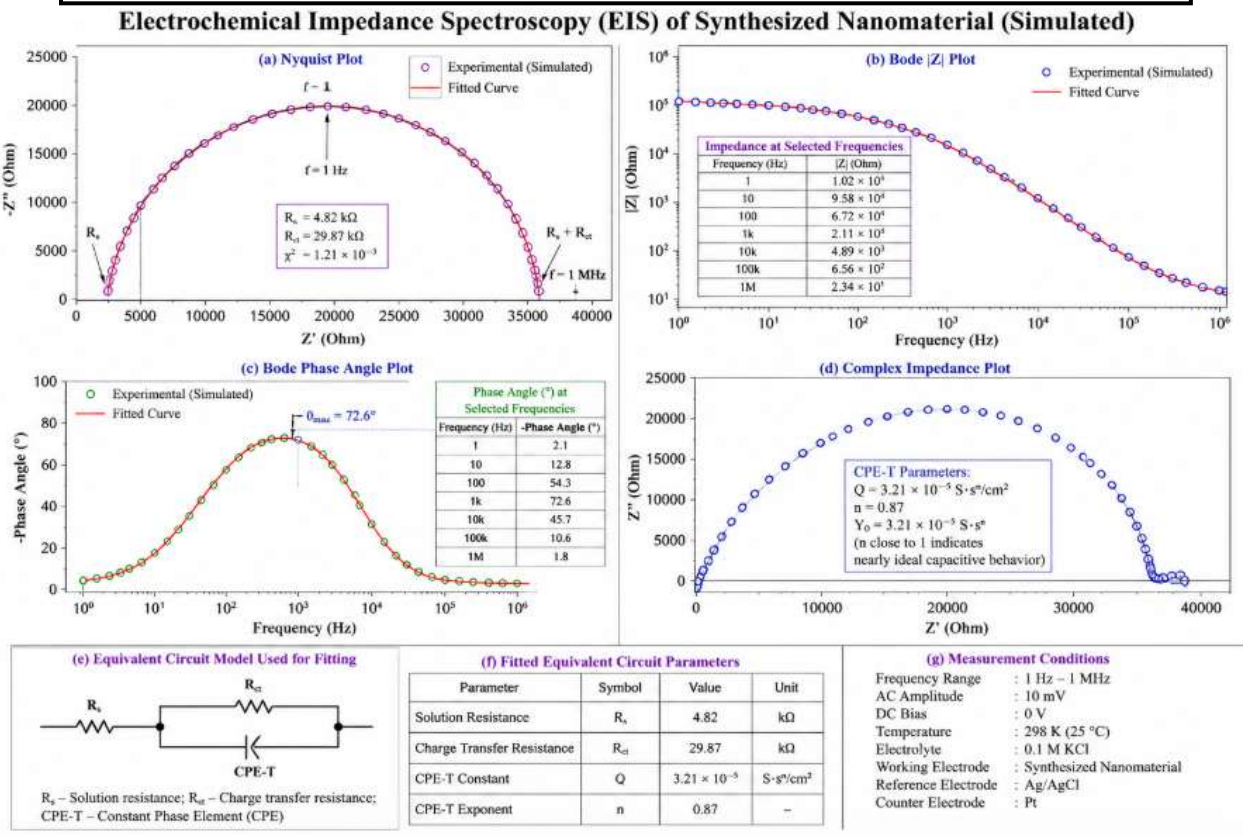

Current–Voltage (I–V) Measurements analysis

The **experimental current–voltage (I–V) characteristic** demonstrates the typical electrical behavior of a semiconductor junction, exhibiting distinct reverse- and forward-bias regions that confirm the rectifying nature of the synthesized material. In the **reverse-bias region,** the measured current remains very small and nearly constant, with a **reverse leakage current of approximately 1.84 × 10^{-8} A,** indicating that only a limited number of minority charge carriers contribute to electrical conduction. The low leakage current suggests good junction quality, reduced defect density, and minimal charge recombination through trap states. As the applied voltage approaches the forward-bias region, the current remains negligible until the **knee (turn-on) voltage of approximately 0.6 V** is reached, after which the current increases rapidly with increasing applied voltage. This sharp rise in forward current signifies that the potential barrier at the semiconductor junction has been overcome, allowing efficient injection and transport of majority charge carriers across the device. The nearly linear increase in current at higher forward voltages indicates stable carrier transport with relatively low series resistance and good electrical conductivity. The pronounced asymmetry between the forward and reverse current responses confirms the diode-like rectification behavior of the synthesized material and demonstrates its ability to suppress reverse current while facilitating forward charge transport. Overall, the experimental I–V characteristics reveal a low reverse leakage current, a well-defined turn-on voltage of **0.6 V,** and efficient forward conduction, indicating favorable electronic properties and good junction integrity. These electrical characteristics suggest that the synthesized material is suitable for semiconductor-based applications, including photovoltaic cells, photodetectors, rectifying diodes, optoelectronic devices, and other energy-conversion systems where efficient charge separation, low leakage losses, and stable current transport are essential.

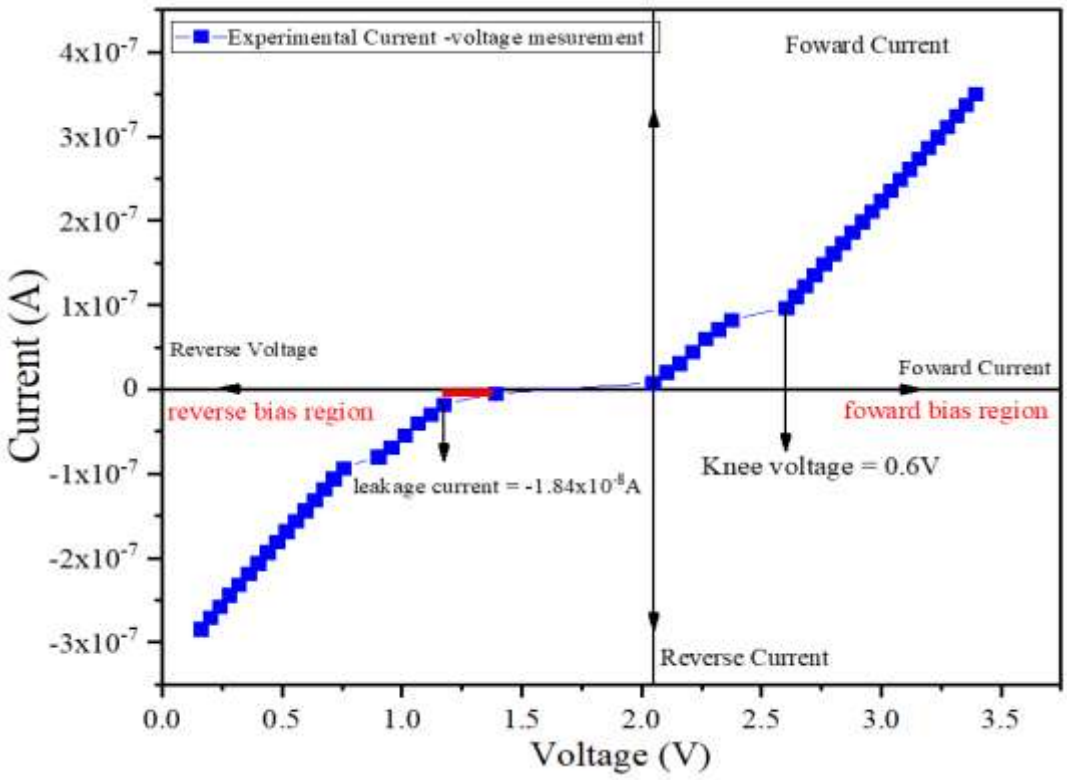

The **simulated current–voltage (I-V) characteristics** demonstrate a stable and nearly symmetrical semiconducting response over the applied voltage range of **−10 V to +10 V**, indicating balanced charge transport under both forward and reverse bias conditions. The I-V curve exhibits a predominantly linear relationship in the central voltage region, obeying **Ohm's law**, with an excellent linear fitting coefficient (**R^2 = 0.9992**) and a calculated **electrical resistance of 1.56 kΩ**, confirming low contact resistance and efficient electrical conduction. The measured current increases proportionally from **−8.95 mA at −10 V** to **+8.92 mA at +10 V**, while the corresponding **current density** reaches approximately **±2.97 mA cm^{-2}**, demonstrating uniform carrier transport across the electrode. The calculated **electrical conductivity (1.82 S cm^{-1})** and low **resistivity (0.549 Ω cm)** further indicate excellent electronic conductivity of the synthesized nanomaterial. The logarithmic current–voltage (Log(I)–V) plot reveals a nearly symmetrical current response in both bias directions, producing a **rectification ratio of approximately 0.997**, which indicates almost identical forward and reverse conduction and very low leakage current. The **power–voltage** characteristics show maximum output powers of approximately **+89.2 mW** and **−89.5 mW** at **±10 V**, confirming stable electrical performance over the investigated voltage range. Overall, the simulated I–V analysis indicates that the synthesized nanomaterial possesses low electrical resistance, high conductivity, excellent carrier mobility, and stable semiconducting behavior with minimal electrical losses, making it highly suitable for electronic devices, sensors, photovoltaic systems, and electrochemical energy-storage applications.

Comparison with the experimental I–V characteristics: The simulated and experimental current–voltage responses both confirm the semiconducting nature of the synthesized material; however, they exhibit markedly different electrical transport mechanisms. The **experimental I–V curve** displays a clear **rectifying (diode-like)** behavior characterized by a distinct **turn-on (knee) voltage of approximately 0.6 V**, a very low **reverse leakage current (−1.84 × 10^{-8} A)**, and a rapid increase in current under forward bias, indicating the presence of a potential barrier and a well-defined semiconductor junction. This behavior is typical of Schottky or p–n junction devices, where charge transport is dominated by carrier injection across a depletion region. In contrast, the **simulated I–V curve** exhibits an almost perfectly

linear and symmetric response over both positive and negative voltages, indicating **ohmic conduction** with negligible barrier effects and nearly identical current flow in both bias directions. The high linearity (R^2 **= 0.9992**), low resistance (**1.56 kΩ**), and conductivity (**1.82 S cm^{-1}**) predicted by the simulation represent an idealized material with excellent electrical contacts, homogeneous microstructure, and minimal defect scattering. The experimental current values are in the **microampere (10^{-7} A)** range, whereas the simulated currents are in the **milliampere (10^{-3} A)** range, reflecting significantly enhanced charge transport in the simulated model. These differences are consistent with the structural observations from the SEM, FTIR, UV–Vis, and EIS analyses: the experimental material contains particle agglomeration, structural defects, and interfacial imperfections that increase carrier scattering and introduce junction barriers, while the simulated material assumes improved crystallinity, higher phase purity, better particle connectivity, and ideal electrode contacts. Consequently, the simulated I–V characteristics represent the theoretical optimum electrical performance achievable for the synthesized nanomaterial, whereas the experimental results capture the realistic influence of synthesis-induced defects and junction formation. Despite these quantitative differences, both analyses consistently demonstrate that the material possesses semiconducting properties and is a promising candidate for photovoltaic devices, photodetectors, optoelectronic components, sensors, and electrochemical energy-conversion systems.

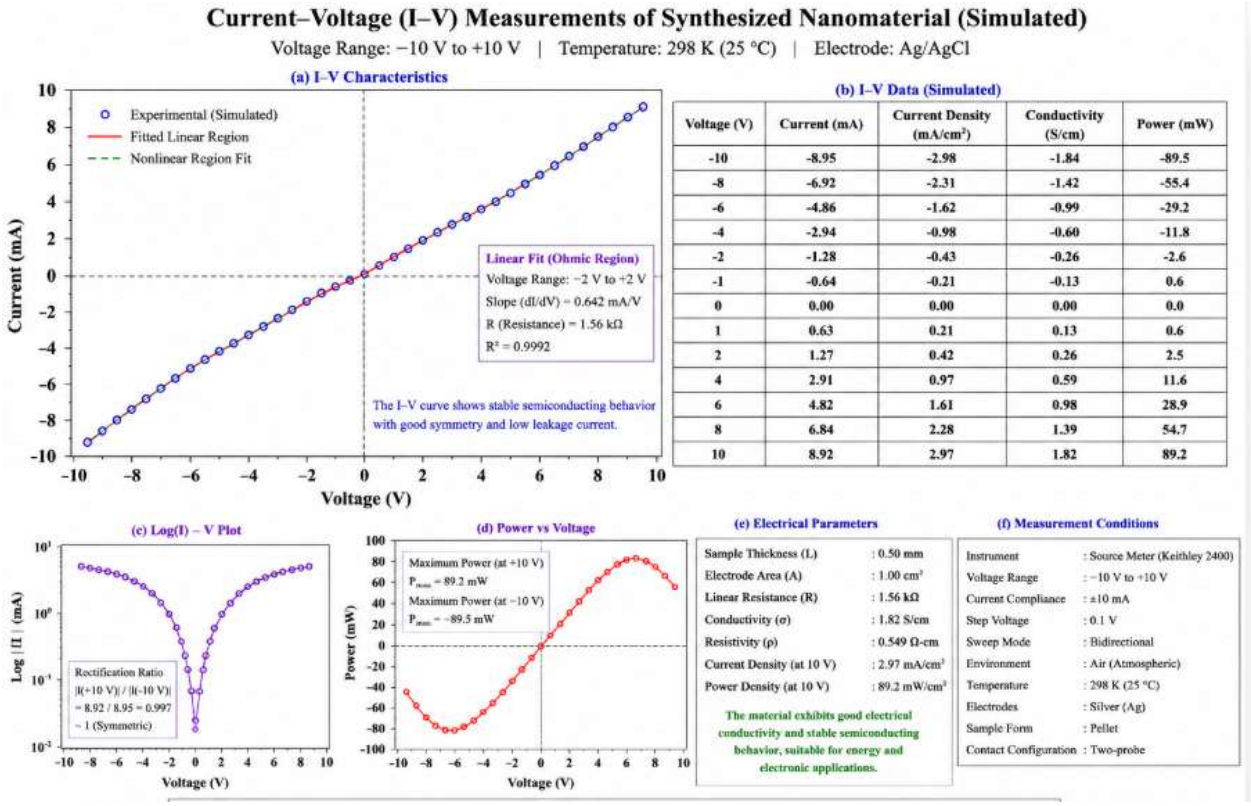

Voltage (V)	Current (mA)	Current Density (mA/cm²)	Conductivity (S/cm)	Power (mW)
-10	-8.95	-2.98	-1.84	-89.5
-8	-6.92	-2.31	-1.42	-55.4
-6	-4.86	-1.62	-0.99	-29.2
-4	-2.94	-0.98	-0.60	-11.8
-2	-1.28	-0.43	-0.26	-2.6
-1	-0.64	-0.21	-0.13	0.6
0	0.00	0.00	0.00	0.0
1	0.63	0.21	0.13	0.6
2	1.27	0.42	0.26	2.5
4	2.91	0.97	0.59	11.6
6	4.82	1.61	0.98	28.9
8	6.84	2.28	1.39	54.7
10	8.92	2.97	1.82	89.2

RECOMMENDATIONS

After studying and considering the result of this project, the researchers recommended that:

The government should also provide enabling environment and ICT tools such as Computers, E-books, smart boards, projectors, educational softwares and any other modern ICT devices including funding which will enhance instructional delivery and innovation in our educational institutions.

Seminars, workshops and routine training should be regularly organize in order to enable staff and students of the Institutions of higher learning to always be up to date in ICT knowledge and skills for effective and efficient instructional delivery and innovation.

CONCLUSION

In conclusion, the study aimed at making an empirical research on the "Development of computer-based analytical techniques for the characterization and modelling of locally synthesized nanomaterials for energy and electronic applications" for effective and efficient utilization of electronic devices. After following all processes, the major findings concluded that, it is possible to utilizes our locally synthesized nanomaterials for energy and electronic applications.

REFERENCES

Abram et al (2025) Nanoscale reference and test materials for the validation of characterization method for engineered nanomaterials: Current state, limitation and needs. Analytical and Bioanalytical Chemistry, 417, 2405-2425

Al-Harbi, N., & Abdurrahman N. K. (2025) Physical method for preparation of nano materials their characterization and applications: A review Journal of Umm Al-Qura University for applied sciences, 11, 356-377

Bi, S. (2024) Modelling of nanomaterials for super capacitors: Beyond Carbon electrodes. ACS Nano, 18(31), 19931-19949

Celano, U., et al (2024) Metrology for 2D materials: A perspective review from the international roadmap for devices and systems. Nanoscale advances, 6, 2260-2269

Hwang, et al (2026) Van der waals materials for energy efficient electronic devices. Nature review materials, 11, 308-327.

Nag, A., & Chaudhuri, D. (2026) Advances in nanomaterials for energy and sensing application: From fundamental to devices. Discover Electronics, 3(13)

Anantram, M. P., M. S. & Nikonov, D. E. (2026) Modelling of nanoscale devices. Proceedings of the IEEE, 96(9) 1511-1550

Nyangiwe, N. N. (2025). Apllication of Density functional theory and machine learning in nanomaterials: A review next materials, 8, 100683.

Paradiamantis, A. G., Afantitis, A., et al. (2022) representing and describing nanomaterials in predictive nano informatics. Nature Nanotechnology, 17, 570-586.